

Remarkable cryogenic strengthening and toughening in nano-coherent CoCrFeNiTi_{0.2} high-entropy alloys via energetically-tuning polymorphous precipitates

J.L. Yuan^a, Y.C. Wu^a, P.K. Liaw^b, J.H. Luan^c, Z.B. Jiao^d,
J. Li^e, P.D. Han^a, J.W. Qiao^{a,*}

^aLaboratory of High-Entropy Alloys, College of Materials Science and Engineering, Taiyuan University of Technology, Taiyuan 030024, China

^b Department of Materials Science and Engineering, The University of Tennessee, Knoxville, TN, 37996-2200, USA

^c Department of Materials Science and Engineering, City University of Hong Kong, Hong Kong, China

^d Department of Mechanical Engineering, The Hong Kong Polytechnic University, Hong Kong, China

^e State Key Laboratory of Advanced Design and Manufacturing for Vehicle Body, Hunan University, Changsha, 410082, PR China

Abstract

In the present work, three kinds of precipitates with different morphologies, structures, sizes, and volume fractions were obtained via energetically-tuning the microstructures of the nano-precipitated CoCrFeNiTi_{0.2} high-entropy alloy (HEA). Subjected to the heavy cold rolling immediately after homogeneous precipitation, L1₂ structured spherical nano-particles with an average size of 16.5 nm rapidly grow into 200 nm-sized spherical ones due to Ostwald ripening. On the other hand, superfluous

* Corresponding author. E-mail: qiaojunwei@gmail.com

mechanical energy storage energetically facilitates the phase transformation from spherical $L1_2$ to rod-shaped $D0_{24}$ structures for initially formed nano-precipitates. Besides, some other newly formed nano-precipitates with an average size of 6.5 nm are available, originating from heavily plastically deformed-induced nucleated sites. Multi-scale precipitates interact with dislocations in different ways. The strengthening provided by dislocations cutting through smaller nano-particles and bypassing grown ones account for 57.7% and 42.3% of precipitation strengthening, respectively, while rod-shaped precipitates can act as equivalent interfaces to hinder dislocation movement. Their synergistic effect has achieved remarkable strengthening and toughening. Specially, dislocation slips dominate at 298 K, while stacking faults (SFs) assist plastic deformation at 77 K. Compared with 298 K, the yield strength (YS) and ultimate tensile strength (UTS) of the current HEAs at 77 K are increased by 38.9% and 38.2% to 1 GPa and 1.5 GPa, respectively, and the tensile strain is slightly increased to 35% instead of loss, realizing excellent strength and plasticity combination. In view of the obvious difference of YS between the two temperatures, a theoretical model is established based on the quantitative relationship between temperatures and four strengthening sources, and the plastic deformation is effectively predicted by the Whitehouse-Clyne model. This strengthening strategy of energetically-tuning polymorphous precipitates provides the basic guidance to develop high-performance nano-precipitated alloys. The current strengthening and plasticity models can be employed to well predict the mechanical properties of such kinds of alloys at cryogenic temperatures.

Keywords: High-entropy alloys; Coherent; Strengthening; Cryogenetic; Deformation mechanisms

1. Introduction

It has to be said that as one of the important breakthroughs in the field of metals and alloys in recent decades, high-entropy alloys (HEAs) [1-7] develop a school of their own among multitudinous metallic materials by introducing ‘chemical disorder’ and ‘high mixing entropy’ effects through multi-component mixing. Their excellent comprehensive properties, including mechanical and functional properties, make them possess great potential and competitiveness in the application fields of heat-resistant and wear-resistant coatings, magnetic materials, new energy materials, space technology, and so on, and open up a blue ocean for the development of late-model alloys [8,9].

Extensive work has been done on face-centered-cubic (fcc) HEAs because of their excellent toughness and work-hardening ability [10,11], but it is a great challenge to be applied in the field of load-bearing materials due to their inherent low strengths [12]. Great efforts, such as solution strengthening, interface engineering, dislocation strengthening [13-20] etc., have been tried to overcome this Achilles' heel of the strength-ductility trade-off. However, there seems to be a gap between them and high-performance structural materials. Recently, it has been reported that strengthening the matrix alloy by the precipitation of coherent ordered secondary phases at nano scale is promising [21]. For instance, the strength increment of the

$\text{Co}_{37.6}\text{Ni}_{35.4}\text{Al}_{9.9}\text{Mo}_{4.9}\text{Cr}_{5.9}\text{Ta}_{2.8}\text{Ti}_{3.5}$ HEA with a high-volume fraction of L1_2 phases reaches 770 MPa. Moreover, due to its outstanding resistance to coarsening, the HEA exhibits more attractive high-temperature strength than many superalloys [22]. Two other typical examples are that the yield strengths (YS) of $(\text{FeCoNi})_{86}\text{Al}_7\text{Ti}_7$ and $(\text{CoCrNi})_{94}\text{Al}_3\text{Ti}_3$ HEAs reported by Yang et al. and Zhao et al., respectively, are over 1 GPa, and both of HEAs have no plasticity loss. Compared with the matrix, the strengths of these precipitate-reinforced HEAs are increased by 5 times and 70%, respectively, but the distinguished tensile strains of 50% and 40% can still be maintained [23,24]. To sum up, this strategy not only solve the long-standing bottleneck of the trade-off between the strength and ductility, but also keeps thermostable in a wide temperature window. It can be attributed to that the enthalpy and free energy in thermodynamics reduces as a result of the ordering transformation and elemental partition, and the interaction between ordered phases and dislocations becomes the main source of strength contributions [23]. It is gratifying that these precipitates-hardened HEAs mentioned above are easy to achieve high strengths and toughnesses even at low temperatures due to the coherency and similar moduli between the matrix and precipitates. Hence, they do not exhibit the ductile-brittle transition fracture behavior as in traditional dilute alloys [25,26]. Moreover, the mechanism upon low-temperature deformation is still unclear.

In the current work, Ti, a strong γ' -forming element, was added to the CoCrFeNi-based alloys. The large atomic-size difference between Ti and other elements increases the lattice distortion, which favourably enhances solution

strengthening [27,28]. Moreover, multi-scale precipitates were achieved by proper thermo-mechanical treatment, and a good combination of mechanical properties was attained. Finally, it is explained that the reason why the alloy has high strength and toughness at low temperatures is that stacking faults (SFs) participate in the coordinated deformation [29]. The current work provides a basic understanding and reference for exploring new low-temperature high-performance alloys.

2. Materials and methods

The ingots with a nominal composition of CoCrFeNiTi_{0.2} (in atomic percent, at. %) were obtained by vacuum arc melting under a Ti-gettered argon atmosphere. Then, the 80 × 10 × 3 mm³ (length × width × thickness) thin plates were prepared by a water-cooled copper mold suction casting method. Each ingot was flipped and re-melted more than five times to ensure the chemical uniformity. The as-cast sheets were homogenized at 1,200 °C for 2 h (denoted as Alloy A hereafter) and aged at 900 °C for 15 min. to obtain the nanoscale precipitate (Alloy B). Subsequently, cold rolling was carried out with a total reduction ratio of 70% (the thickness changed from 3 to 0.9 mm). Finally, after recrystallization annealing at 900 °C for 15 min., a variety of precipitates were obtained (Alloy C). All heat treatments were conducted in air, followed by water quenching.

Dog-bone-shaped specimens with a gauge length of 12.5 mm and cross-section dimension of 3 × 1.5 mm² and 3 × 0.9 mm² were fabricated by electro-discharge machining for uniaxial tensile tests at 298 K and 77 K, respectively,

which were performed on an Instron 5969 universal testing machine with a constant strain rate of $1 \times 10^{-3} \text{ s}^{-1}$. At least three samples were measured in each case to ensure the reliability of the data. Digital image correlation (DIC) was applied to record the continuous deformation of the gauge section during tension, and the data was converted into strain maps by the three-dimensional (3D) test and evaluation software (GOM Correlate).

The phase identification was conducted, using X-ray diffraction (XRD) with Co-K α radiation. The scanning angle range of 2θ is $20^\circ - 100^\circ$. The microstructures and deformation mechanisms of the alloys were characterized by the electron-backscattered diffraction (EBSD), scanning electron microscopy (SEM, Phenom XL), and transmission electron microscopy (TEM, JEM-2100(HR)) with selected area diffraction patterns (SADPs). For EBSD and SEM analyses, the surfaces of the samples were ground to 2,000 grit SiC paper, and then electrochemically polished with a $\text{HClO}_4:\text{C}_2\text{H}_6\text{O} = 1:9$ solution (in a volume percent, vol.%) with a direct-current (DC) voltage of 20 V at 298 K. For the TEM analysis, the samples were first mechanically ground to a thickness below 50 μm and then punched into 3 mm-diameter discs. Finally, the discs were thinned to a thickness of electron transparency by twin-jet electro-polishing at a DC voltage of 20 V and a temperature of around -10°C , using the same electrolyte. Needle-shaped specimens required for atom probe tomography (APT) were fabricated by lift-outs and annularly milled in a FEI Scios focused ion beam/scanning electron microscope (FIB/SEM). The APT characterizations were performed in a local electrode atom probe (CAMEACA LEAP

5000 XR). The specimens were analyzed at 70 K in a voltage mode, at a pulse repetition rate of 200 kHz, a pulse fraction of 20%, and an evaporation detection rate of 0.2% atom per pulse. The data-analysis workstations, AP Suite 6.1, was used for creating the 3D reconstructions and data analysis.

3. Results

3.1 Microstructures

The XRD and SEM images of the alloys in three states, namely the homogenized (Alloy A), aged (Alloy B), and recrystallization-annealed (Alloy C) materials, respectively, are presented in Fig. 1. Only one set of fcc diffraction peaks can be identified in Alloy A, which indicates that it is a single-phase structure. In contrast, weak additional diffraction peaks are detected in both Alloys B and C. However, the intensities of these peaks are very low, and the number is really small. Hence, it is difficult to determine the phase structure. It can be proved that this trend is ascribed to the existence of precipitates demonstrated later, since the extremely-low negative enthalpy of mixing between Ni-Ti and Co-Ti atomic pairs (- 35 kJ/mol and - 28 kJ/mol, respectively) makes a strong tendency to form precipitates during rapid quenching.

The microstructures of the three alloys were characterized by SEM. From microstructural observations, Alloy A is equiaxed with an average grain size of about 54 μm , and the dispersed dark spots are Ti-enriched particles generated during casting. After aging at 900 °C for 15 min., the grain size of Alloy B is slightly increased to

about 71 μm . However, the formation of precipitates different from Alloy A cannot be found from the SEM images due to its small size, but the TEM image (Fig. 1e₁) indicates the emergence of spherical precipitates. The diameter and volume fraction of spherical particles are about 16.5 nm and 6.8%, respectively. Upon cold rolling and subsequent recrystallization annealing, the microstructure of Alloy C consists of both spherical and rod-shaped precipitates with an evenly-cross distribution within the fcc matrix. It is worth noting that the spherical precipitates are not the same as those in Alloy B.

The EBSD images of the three alloys are displayed in Fig. 2. The grain size of Alloy A increases from 20 to 200 μm , and the sample presents a preferential orientation relationship of $\langle 001 \rangle // \text{ND}$ (normal direction), which may be due to the orientation nucleation and growth caused by the directional heat dissipation during casting (Fig. 2a). Alloy B also has larger equiaxed grains with an uneven size (Fig. 2b). It is obvious that the grain boundary of Alloy C cannot be observed directly by SEM, but the EBSD image of Alloy C clearly shows the structure of basically-complete recrystallization (Fig. 2c), and the formation of twins ($\Sigma 3 \langle 111 \rangle$) can be found from its grain-boundary diagram, which is almost absent in Alloys A and B (Fig. 2d). The microstructure of Alloy C was further analyzed by TEM. As shown in Fig. 3a, the regions with rod-shaped and spherical precipitates are labeled as Regions I and II, respectively. The SADPs on the right confirm that the matrix is indeed an fcc structure, and additional blur points appear in the diffraction spots corresponding to the two regions. Furthermore, there are weak "awn lines" (symbols

of SFs) and twin spots symmetrical to the matrix in SADPs. This trend is due to that the twins and SFs generated by the activation of the residual stress after thermo-mechanical treatments provide sites for the preferential nucleation of precipitates. Furthermore, it is verified that these two precipitates have different crystal structures. Among them, the rod-shaped precipitate is a η - Ni₃Ti [D0₂₄, a hexagonal-close-packed (hcp) structure] phase, while the spherical particle is a L1₂ γ' -Ni₃Ti (fcc) phase. Next, high-resolution TEM (HRTEM) images of these two precipitates provide a more intuitive understanding of the matrix-precipitate interface structure, as presented in Figs. 3b₁ and c₁. Combined with their fast Fourier transform (FFT) images (Figs. 3b₂ and c₂), it can be concluded that they are secondary phases with different morphologies and structures. The nano size and ordering effect lead to weak scattering, which makes the diffraction peaks not clearly displayed from XRD patterns [30]. The inverse fast Fourier transform (IFFT) images (Figs. 3b₃ and c₃) show the characteristic contrast of bright and dark lines, which is generally caused by the lattice distortion in the precipitates and their long period arrangement. Figure 3d is an enlarged view of Region III in Fig. 3c, in which the finer spherical precipitates are the same as those in Alloy B, but they are newly formed due to the high-energy-driving force during recrystallization annealing after cold rolling. The corresponding diffraction pattern indicates that it is a L1₂ phase. The size and volume fraction of the small spherical particles become 6.5 nm and 3.95%, respectively. Therefore, three precipitates with different crystal structures coexist in the recrystallized alloys. The grain size, diameter, and volume fraction of precipitates for

the three alloys are summarized in Table 1. Figure 4 schematically exhibits the different microstructures of the every three alloys. Alloy A is a single-phase fcc structure. In Alloy B, small spherical precipitates appear within the fcc matrix, while rod-shaped, large and small spherical precipitates coexist in Alloy C, accompanied by annealing twins and SFs.

The origin of the three precipitates can be explained as follows. Large spherical particles in Alloy C are formed by the growth of small spherical particles in Alloy B through the Ostwald ripening mechanism, while rod-shaped precipitates are further transformed from larger spherical particles, which are usually generated at grain boundaries. At the same time, the rolling structure, such as incompletely recovered shear bands provides a large number of new nucleation sites, which makes small spherical particles precipitate again during recrystallization annealing. The spherical particles nucleated first grow rapidly under the effect of strain energy, and then nucleated particles grow slowly. Therefore, the sizes of the two spherical precipitates in Alloy C are quite different. Similar to the Fe- (25 - 30) Ni-Ti alloy, the precipitates undergo an $L1_2 \gamma' - Ni_3Ti$ metastable state and then changes to a $\eta - Ni_3Ti$ - a stable state [31]. In the current HEAs, the precipitation of the coherent $L1_2$ phase is more favorable in kinetics. Hence, it appears first, and the transformation from the $L1_2$ to η phase is due to the introduction of extrinsic stacking faults (ESFs) in the $L1_2$ phase. The ESF comes from the climb of the Frank sessile dislocation, that is, the structure is changed by repeatedly adding (0001) planes from the $L1_2$ structure. Figure 5 illustrates this transition. Figure 5a is the planar stacking sequence of the $L1_2$ phase,

which can be expressed as ABCABC..., and when a Frank edge dislocation climbs continuously to produce a layer-A atomic plane, namely B(A)C(A)B..., or adds a layer-A every other group, namely ABAC(A)B....The stacking sequence will change to ABACABAC..., i.e., the stacking sequence of the hcp structure. Some studies show opposite results for the enthalpies of the formation of the two phases [32,33]. Based on this process, it is assumed that their phase stabilities are similar. Hence, the volume fractions of the two phases in Alloy C are almost the same (the volume fraction of the rod-shaped precipitates is 7%). In addition, the orientation relationships between the precipitates and matrix usually follow $\{0001\} \eta // \{111\} \gamma$ and $\langle 2110 \rangle \eta // \langle 011 \rangle \gamma$, while the spherical L1₂ phase and the matrix are $\{001\} \gamma' // \{002\} \gamma$ and $\langle 011 \rangle \gamma' // \langle 011 \rangle \gamma$.

In order to further quantitatively analyze the chemical composition and elemental distribution of the matrix and precipitates, 3D-APT reconstructions of alloys is conducted, and the results are presented in Fig. 6. Figures. 6a and c are atom maps of five elements in Alloys B and C, respectively. The spherical particles rich in Ni and Al are uniformly embedded in Alloy B, and the average size is about 16.93 nm, which is well consistent with the TEM results. Due to the large size of the rod-shaped precipitate in Alloy C, it can only be partially displayed, but the corresponding iso-concentration surface clearly depicts the outline of newly-nucleated small spherical particles. It can be seen intuitively that the spherical particles in Alloy C are significantly smaller than those in Alloy B, and the volume fraction is greatly reduced, which further verifies the above TEM analysis. Figures. 6b and d are proximity

histograms constructed across the interface between the matrix and precipitates, which can be used to further analyze the elemental distribution. Among them, Ni and Ti have a strong tendency to be distributed into these two precipitates, and Co is partially depleted, while Fe and Cr are almost completely depleted. The precise compositions of the matrix, small spherical particles in Alloy B and rod-shaped precipitates in Alloy C are listed in Table 2. The compositions of the two precipitates veil slight differences, in agreement with the origin of three precipitates. Small spherical particles nucleated first grow rapidly and then change into rod-shaped precipitates, and some small spherical particles are precipitated again in Alloy C at the same time. Therefore, they are only precipitates with different morphologies and structures but the same compositions. Generally, the sites of Co and Cr can replace Ni and jointly occupy the A site of the A_3B type precipitates, while Fe can replace both lattice sites. As a consequence, the stoichiometry can be roughly expressed as $(Co,Cr,Fe,Ni)_3(Fe,Ti)$.

3.2 Tensile properties at 298 K and 77 K

Typical engineering stress-strain curves of the three alloys at 298 K and 77 K are exhibited in Figs. 7a and b, respectively. At 298 K, the YS and UTS of Alloy A are 280 MPa and 650 MPa, respectively, and the elongation (EL) at break is 47%. After aging, the YS and UTS of Alloy B increase by 110% and 46% to 580 MPa and 950 MPa, respectively, and the tensile strain decreases slightly, but it can still maintain 27%. Compared with Alloy B, the YS and UTS of Alloy C are enhanced by 140 MPa and 135 MPa, respectively, to 720 MPa and 1,085 MPa, but the plasticity is

not lost, up to 30%. The strength of the alloy at 77 K is stronger than that at 298 K to a certain extent, while the tensile strain does not decrease but increases. Especially, the YS of Alloy C reaches 1 GPa, the UTS is 1.5 GPa, and the EL is 35% at 77 K, showing the most excellent strength-plasticity combination. This feature is opposite to the ductile-brittle transition in most conventional traditional alloys. Figure 7c presents the work-hardening capacity of Alloy C at 298 K and 77 K through the strain-hardening rate ($d\sigma/d\varepsilon$, where σ and ε are the true stress and true strain, respectively) as a function of true strain. The work-hardening rate at 77 K is slightly higher than that at 298 K because SFs, as a main deformation mode, enhances the work-hardening ability of the alloys. At the initial stage of plastic straining, the work-hardening rate drops sharply, which corresponds to the dislocation strengthening, described by the classical Taylor model [34]. When the strain is further increased, the work-hardening rate decreases slowly, which can be attributed to the formation of substructures, such as dislocation cells (DCs), dislocation walls (DWs), and so on [35,36]. These dislocation substructures proliferate, and the grains refine again as the plastic deformation continues, which shortens the average free path of dislocation motion and produces successive work hardening. The persistent change of the strain field during tension was recorded by DIC strain mapping, as shown in Fig. 7d. The alloy has a uniform elongation until final fracture. The YS, UTS, and EL of the three alloys at two temperatures are summarized in Tables 3 and 4. A large number of dimples appear on the fracture surface of the alloys at both temperatures, indicating typical ductile fracture. In contrast to 298 K, the dimple size is smaller, and the

density is higher at 77 K (not shown here). Figure 8a summarizes the tensile strength and total elongation of Alloy C, and makes a direct comparison with the properties of some other traditional and advanced alloys, including advanced steels, commercial superalloys, medium-entropy alloys (MEAs), solution-strengthened (SS), and precipitation-strengthened (PS) HEAs [37-45]. The UTS of traditional aluminum and magnesium alloys is limited to about 200 ~ 600 MPa, with a moderate plasticity, and the tensile strain is usually less than 30%. In contrast, the strength of the manganese steel can reach 4 times of them, but the plasticity is largely lost, only 10%. There are also some TRIP steels, dual-phase steels, and ferritic steels in the area between their performance distributions. The strength and plasticity are neutralized, but there is still an inverse relationship. The results show that the properties of the alloy strengthened by solute atoms are widely distributed, the strength is about 200 ~ 1,000 MPa, and the plasticity is extended from 5% to 100%. They are all in the upper left and lower halves of the picture, and the upper right corner is still blank. The precipitation-hardened Alloy C adds a great amount of color to the high-performance area in the upper right corner. The toughness of the alloys is further evaluated by comparing YS and the product of strength and elongation ($UTS \times EL$). As shown in Fig. 8b, the YS of Alloy C at 77 K is 1 GPa, and the $UTS \times EL$ is 52.5 GPa%. The $UTS \times EL$ of the alloys with the equivalent strength is only half of Alloy C, while the YS of the alloys with the equivalent $UTS \times EL$ is only one third of it, which once again proves the excellent mechanical properties of Alloy C.

4. Discussion

4.1 Deformation mechanisms

In order to explore the deformation mechanisms of the Alloy C at different temperatures, the samples after tensile rupture were analyzed by TEM. The fracture morphologies at 298 K are revealed in Fig. 9. It is clear that the dislocation slips dominate upon tension. Rod-shaped precipitates become a powerful obstacle to dislocation movement and accumulate dislocations, which is similar to DWs (Fig. 9a). Besides that, spherical particles work in pinning dislocations and hindering the grain-boundary migration to a large extent, and act as dislocation sources to cause continuous strengthening (Fig. 9b). Extensive cross-slip, dislocation entanglement, and dislocation cells lead to successive plasticity. Upon ever-increasing deformation, the cellular substructure is consecutively refined. Hence, the number increases, and the size decreases, which reduces the average free path and increases the resistance of dislocation movement, rendering that the flow stress of the alloys during plastic deformation is effectively raised (Fig. 9c). Compared with 298 K, the properties of the alloys at 77 K are substantially improved, since SFs promote dislocation pile-ups as another auxiliary deformation mechanism, indicated in Fig. 10. At the early stage of plastic deformation, the leading $1/2 \langle 110 \rangle$ perfect dislocation in the dislocation array dissociates into $1/6 \langle 112 \rangle$ and $1/3 \langle 121 \rangle$ partials (the successive slip and propagation of the $1/3 \langle 121 \rangle$ dislocation is the origin of micro-twins, as reported before [46]). When the resistance caused by dislocation stacking is enough to resist its further slip, a new slip system will be activated. The $1/2 \langle 110 \rangle$ dissociated into a pair of $1/6$

$\langle 112 \rangle$ and SFs, which are known as extended dislocations. The SFs are blocked by rod-shaped precipitates and large spherical particles, or sheared by small spherical particles. The extended dislocations on the two intersecting (111) planes interact with each other to form a sessile stair-rod dislocation, i.e., the Lomer-Cottrell (L-C) lock (Fig. 10e) [47]. The multi-layer L-C locks intersect each other drastically to form a SF network, subdividing grains again to produce a dynamic Hall-Petch (H-P) effect. An analogous phenomenon has been revealed previously [48,49]. Due to the high stability of the dislocation structure, it is hard for the $1/6 \langle 112 \rangle$ Shockley partials to cluster and merge into an original non-extended state. In that way, when the dislocation sliding is impeded, and the plastic straining is coordinated by cross-slip, more external force is needed to heighten the strength [50,51]. Figure 10f manifests the dislocation bypassing the large spherical particles.

SFs are determined by the temperature-dependent stacking fault energy (SFE), and has a linear relationship. Different from the current HEAs, the deformation of the CoCrFeNi HEA with a low SFE (13 mJ/m^2) at 77 K is mediated by twinning [52]. This is because that the precipitation of nanoscale spherical particles reduces the matrix channel, and the rod-shaped precipitates indirectly diminish the grain size, meanwhile the SFE of these precipitates with high ordering is much greater than that of the matrix [53]. Under the joint action of these precipitates, the nucleation driving force for twinning is increased enormously. Hence, twinning is not easy to be activated. Here, the SFE of the alloys with the matrix composition of $\text{Co}_{24.5}\text{Cr}_{25.5}\text{Fe}_{27}\text{Ni}_{20.5}\text{Ti}_{2.5}$ at 77 K is 65.6 mJ/m^2 through molecular dynamics

simulations, as shown in Fig. 11b. Hence, the critical twinning stress, σ_{tw} , reaches 2,730 MPa (calculated by the equation of Byun [54], $\tau_{tw} = \frac{2\gamma_{isf}}{b_p} = 892.5$ MPa, where γ_{isf} is the intrinsic stacking fault energy, and $b_p \approx 0.147$ nm is the value of the Shockley partial dislocation), while the maximum true stress during the whole tension is only slightly more than 2,000 MPa (Fig. 11a), sufficient for the suppression of twinning. On the contrary, the extremely-low SFE of the CoCrFeNi HEA makes its σ_{tw} of only 635 MPa, which is prone to achieve. Hence, twins favourably appear. Moreover, it can be found that the addition of Ti has a great impact on the SFE of the matrix. Therefore, it can be inferred that the SFE of precipitates with a high content of Ti is several times that of the matrix. The large difference of SFE between the matrix and precipitates would cause the change of the extended dislocation energy and produce additional force to hinder dislocation movement. The UTS of Alloy C at 77 K is more than 400 MPa higher than that at 298 K, which is mainly due to the contribution of SFs [29].

4.2 Strengthening mechanisms

The YS of polycrystalline alloys is usually the sum of four contributions, i.e., solid-solution strengthening ($\Delta\sigma_s$), grain-boundary strengthening ($\Delta\sigma_g$), dislocation strengthening ($\Delta\sigma_d$), and precipitation strengthening ($\Delta\sigma_p$). In the current CoCrFeNiTi_{0.2} HEAs, the YS can be expressed as:

$$\Delta\sigma_{0.2} = \sigma_0 + \Delta\sigma_s + \Delta\sigma_g + \Delta\sigma_d + \Delta\sigma_p \quad (1)$$

where σ_0 is the lattice-friction stress. In this alloy, the addition of Ti will increase the lattice distortion and enhance solid-solution strengthening, as the atomic radius of Ti

is much larger than the other four elements. Since the concepts of "solute" and "solvent" in HEAs cannot be clearly distinguished, it is challenging to adopt the traditional solid-solution strengthening theory. Here, the strength difference between the Alloy A and single-phase CoCrFeNi HEA under the same conditions is regarded as the contribution of $\Delta\sigma_s$. Therefore, the CoCrFeNi alloy (Alloy D) was prepared by homogenizing at 1,200 °C for 2 h, and its YS is 170 MPa. However, the grain size of Alloy D is larger than that of Alloy A, which is about 155 μm . Hence, it is necessary to employ the H-P equation to describe the grain-size dependence on $\Delta\sigma_g$:

$$\Delta\sigma_g = K_y \cdot (d_2^{-1/2} - d_1^{-1/2}) \quad (2)$$

where K_y is the strengthening coefficient ($K_y \approx 226 \text{ MPa} \cdot \mu\text{m}^{1/2}$ from the CoCrFeMnNi system [14]), and d is the average grain size. Substituting the values of d for Alloys A and D, the $\Delta\sigma_g$ caused by grain refinement is 12.6 MPa. Thus, the contribution of $\Delta\sigma_s$ is $280 - 170 - 12.6 = 97.4 \text{ MPa}$, and then $\sigma_0 = 280 - 97.4 = 182.6 \text{ MPa}$ can be obtained.

Compared with Alloy A, the YS increment of Alloy B is the result of the precipitation strengthening increment offsetting the grain-boundary strengthening loss caused by the increase of the grain size. Substituting the value, d , of Alloys A and B into Equation 2, the $\Delta\sigma_g$ is - 3.9 MPa. The precipitates can be divided into deformable and non-deformable particles according to their characteristics. Hence, there are two interaction modes, namely shear and Orowan bypass mechanisms to strengthen the alloys. When the particle size is small and coherent with the matrix, the shear mechanism plays a leading role, and vice versa. Coherent strengthening ($\Delta\sigma_{CS}$),

modulus strengthening ($\Delta\sigma_{MS}$), and ordered strengthening ($\Delta\sigma_{OS}$) are the main sources of strengthening, caused by the shear mechanism [55]. The former two occur before the dislocation passes through the precipitates, while the latter exists during shearing. The larger of $\Delta\sigma_{CS} + \Delta\sigma_{MS}$ and $\Delta\sigma_{OS}$ represents the strength increment. They can be calculated by the following formula:

$$\Delta\sigma_{CS} = M \cdot \alpha_\varepsilon (G \cdot \varepsilon_c)^{\frac{3}{2}} \left(\frac{rf}{0.5Gb} \right)^{\frac{1}{2}} \quad (3)$$

$$\Delta\sigma_{MS} = 0.0055M (\Delta G)^{\frac{3}{2}} \left(\frac{2f}{G} \right)^{\frac{1}{2}} \left(\frac{r}{b} \right)^{\frac{3m-1}{2}} \quad (4)$$

$$\Delta\sigma_{OS} = 0.81M \frac{\gamma_{APB}}{2b} \left(\frac{3\pi f}{8} \right)^{\frac{1}{2}} \quad (5)$$

where M is the Taylor factor (3.06 in the fcc phase) [56], α_ε is a constant of 2.6, $\varepsilon_c = \frac{2}{3} \varepsilon = \frac{2}{3} \frac{\Delta a}{a} = 0.002$ is the constrained lattice-mismatch strain, α is the lattice constant, r and f are the average radius and the volume fraction of precipitates, respectively, $G = 84$ GPa is the shear modulus of the matrix ($G = 77$ GPa for precipitates, adopted from Ni₃(Al,Ti) [39,57]), $b = \frac{\sqrt{2}}{2} a = 0.253$ nm is the Burgers vector, m is a constant of 0.85, and $\gamma_{APB} = 200$ mJ/m² is the antiphase-boundary energy of precipitates [58].

The diameter of small spherical precipitates in Alloy B is only 16.5 nm. Hence, the shear mechanism is selected for calculations. The values of $\Delta\sigma_{CS}$, $\Delta\sigma_{MS}$, and $\Delta\sigma_{OS}$ are 127.7 MPa, 33.2 MPa, and 281.3 MPa, respectively, so that the contribution of precipitation strengthening is 281.3 MPa. The sum of the two parts is

281.3 - 3.9 = 277.4 MPa, and the experimental strength increment is 300 MPa, which is in perfect agreement with each other.

As for Alloy C, the interaction between three different precipitates and dislocations is different. For small spherical particles, the effect of the shear mechanism is considered, which is the same as that of Alloy B. The results of the three parts are 60.5 MPa, 19.4 MPa, and 212.7 MPa, respectively. Hence, the strength contribution of 212.7 MPa is provided. For larger spherical precipitates, the bypass mechanism is adopted. The strength increment, $\Delta\sigma_{orw}$, can be expressed as [59]:

$$\Delta\sigma_{orw} = M \frac{0.4Gb}{\pi\sqrt{1-\nu}} \frac{\ln(2r_m/b)}{\lambda_p} \quad (6)$$

where $\nu = 0.31$ is the Poisson's ratio, $r_m = \left(\frac{2}{3}\right)^{0.5} r$, and $\lambda_p = 2r_m(\sqrt{\pi/4f} - 1)$ is the spacing of precipitates. Thus, the large spherical particles provide the strength contribution of 155.7 MPa. Finally, for the rod-shaped precipitates, the length can reach several microns, it is difficult for the dislocations to cut through, and let alone bypass them. Consequently, it is equivalent to the sub-grain boundary, and the effect of $\Delta\sigma_g$ is considered here. The specific methods are described as follows. Several SEM images of different areas were selected for statistics. As shown in Fig. 12a, each graph is divided into 12 equal parts, and then the number of segments of 12 straight lines truncated by rod-shaped precipitates, and the average number of interrupted precipitates are calculated. Finally, the average values of these two groups of data are obtained [60]. These rod-shaped precipitates are equal to the sub-grain boundary in Fig. 12b, and the equivalent grain size is 7 μm . Thus, the value of $\Delta\sigma_g$ is 54.7 MPa.

The sum of these three parts is 423.1 MPa. The experimental strength increment is 440 MPa, which is also fairly close to the predictions, and the rest is the contribution of $\Delta\sigma_d$. The strengthening contributions of various precipitates in Alloy B and C are given in Tables 5 and 6.

The YS of most fcc-based alloys is obviously temperature-dependent, and it is no exception in the current fcc HEAs [39, 61-64]. Here, taking Alloy C as an example, the reasons for this difference are briefly analyzed. Firstly, considering the influence of the temperature on σ_0 , the relationship between σ_0 and the temperature can be expressed as the following formula [39]:

$$\sigma_0(T) = \frac{2G}{1-\nu} \exp\left(\frac{-2\pi\omega_0}{b}\right) \exp\left(\frac{-2\pi\omega_0}{bT_m} T\right) \quad (7)$$

where ω_0 is the dislocation width at 0 K, and T_m and T are the melting temperature and testing temperature, respectively. T_m is calculated to be 1,872 K by the rule of mixing. For CoCrFeNi HEAs, the relationships among G , Young's modulus, E , and T are [65]:

$$G = 89.4 - \frac{13.0}{\left(e^{\frac{373}{T}} - 1\right)} \quad (8)$$

$$E = 226.3 - \frac{30.4}{\left(e^{\frac{384}{T}} - 1\right)} \quad (9)$$

Therefore, G (298 K) = 84.2 GPa, G (77 K) = 89.3 GPa, E (298 K) = 214.7 GPa, and E (77 K) = 226.1 GPa can be obtained. According to $\nu = -1 + \frac{E}{2G}$, ν (298 K) = 0.275, and ν (77 K) = 0.266 are calculated. Substitute σ_0 (298 K) = 182.6 MPa into Equation 7, $\omega_0 = 0.981b$ can be obtained. Then, the $\omega_0 = 0.981b$ is plugged into

Equation 7, σ_0 (77 K) is calculated to be 397.3 MPa. So $\Delta\sigma_0$ (298 K \rightarrow 77 K) is calculated to be 214.7 MPa. $\Delta\sigma_s$ (298 K \rightarrow 77 K) can be determined according to the Fleischer model [66]:

$$\Delta\sigma_s = M \frac{G\varepsilon_s^2 c^{\frac{3}{2}}}{700} \quad (10)$$

where ε_s is the interaction parameter, and the influence of the temperature on it can be ignored, and c is the solute atomic concentration. It can be obtained from Equation 10 that the contribution of $\Delta\sigma_s$ mainly comes from the increase of G . Hence,

$$\sigma_s(77\text{K}) = \frac{\sigma_s(298\text{K}) \times G(77\text{K})}{G(298\text{K})} = 103.3 \text{ MPa}, \text{ and then } \Delta\sigma_s \text{ (298 K} \rightarrow \text{77 K) is}$$

calculated to be 5.9 MPa. For $\Delta\sigma_{os}$, *APB* is not affected by the temperature. Hence, the effect of small spherical particles is not considered here [67]. For large spherical particles, the two variation factors in the bypass mechanism are G and ν . Thus,

$$\Delta\sigma_{orw}(77\text{K}) = \frac{\frac{G(77\text{K})}{\sqrt{1-\nu(77\text{K})}} \Delta\sigma_{orw}(298\text{K})}{\frac{G(298\text{K})}{\sqrt{1-\nu(298\text{K})}}} = 164.1 \text{ MPa}, \text{ and then } \Delta\sigma_p \text{ (298 K} \rightarrow \text{77}$$

K) is calculated to be 8.4 MPa. The theoretical value of YS of Alloy C at 77 K is 932.1 MPa by summing the above parts, which is only 6.79% different from the experimental result of 1,000 MPa. The difference between the experimental and theoretical values can be attributed to the influence of rod-shaped precipitates, because K_y is more sensitive to the temperature in the contribution of rod-shaped precipitates to strength.

A tremendous amount of literatures have reported the quantitative models of material-strength increments, verified by experiments, but the quantitative study of

plasticity is still immature. Here, a Whitehouse-Clyne model suitable for ceramic particles-reinforced metal-matrix composites seems to be employed to evaluate the fracture strain of Alloy C in the present work [68,69]. Because the rod-shaped precipitates are regarded as a structure similar to DWs, which are usually used to improve the strength, only the effects of two scales of spherical precipitates are considered in this model. The strain level is evaluated by the following formula [70]:

$$\frac{\varepsilon_c}{\varepsilon_m} = (1 - f)(1 + \varepsilon_{cav})(1 - f_{con}) \quad (11)$$

where ε_c and ε_m are the fracture strains of alloys with and without the reinforcing phase, respectively. In the current study, they are the fracture strains of Alloy C and Alloy A, accordingly. $f = 13.95\%$ is the volume fraction of reinforcing phase, that is,

the sum of the volume fraction of the two spherical precipitates, $\varepsilon_{cav} = \frac{f^{\frac{4}{3}}}{s}$ represents

the influence of cavity formation, $f_{con} = \frac{2s}{5(f^{-1} - 1)}$ is the ratio of the constrained to the

matrix volume, and s is the aspect ratio of particles. The average aspect ratio, s_1 , of small particles is equal to 1.167, while the morphology of mature large particles is closer to be oval or cubic with rounded corners. Therefore, the average aspect ratio, s_2 , is larger and equal to 3.335. The weighted average value obtained from the volume fractions (3.95% and 10%) is 2.721. When the fracture strain of Alloy A is known to be 0.47, it is inferred that the theoretical value of the fracture strain of Alloy C should be 0.34, which is approximately consistent with the experimental value. The deviation may mainly come from the influence of the particle size. There is a great difference between the nano-sized particles in Alloy C and the micron scale applicable in the

model. Figure 13 schematically shows the contributions of different strengthening mechanisms and the comparison between theoretical and experimental values. It can be seen intuitively that the predicted YS and EL are in good agreement with the experimental results.

5. Conclusion

In the present work, the CoCrFeNiTi_{0.2} HEA strengthened by polymorphic precipitates was prepared by unique thermo-mechanical treatments, which proved a feasibility of inducing precipitation formation by adding a small amount of Ti. The effect of different precipitates on mechanical properties and the related deformation and strengthening mechanisms were discussed. The conclusions are described as follows:

- a. The alloy homogenized at 1,200 °C for 2 h has a single-phase fcc structure. After being aged at 900 °C for 15 min., coherent spherical particles of several nanometers are precipitated. After 70% cold rolling and recrystallization annealed at 900 °C for 15 min., the small spherical particles in Alloy B grow into large spherical particles of about 200 nm through the Ostwald ripening mechanism, and rod-shaped precipitates are further transformed from large spherical particles. At the same time, small spherical particles are precipitated again during annealing. There are three kinds of precipitates with different morphologies, sizes, volume fractions, and structures.

- b. At 298 K, compared with the homogenized Alloy A, the YS and UTS of the aged Alloy B are increased by 110% and 46% due to precipitates, reaching 580 MPa and 950 MPa, respectively, and the tensile strain can still be maintained by 27%. Compared with Alloy B, the YS and UTS of the recrystallization-annealed Alloy C is increased by 140 MPa and 135 MPa, respectively, reaching 720 MPa and 1,085 MPa and maintaining 30% elongation. At 77 K, the YS and UTS of Alloy C are up to 1 GPa and 1.5 GPa, and the tensile strain is slightly increased to 35%, showing a good strength-plastic bonding ability.
- c. At 298 K, the dislocation slip coordinates the plastic deformation of Alloy C, and at 77 K, the SFs become the auxiliary deformation mode. Small spherical particles are sheared by dislocations and SFs, large spherical particles are bypassed, and rod-shaped precipitates are similar to DWs to block dislocation movement. The synergism of the three different interaction modes achieves the effect of strengthening Alloy C.
- d. A variety of strengthening methods play an important role in Alloy C, among which $\Delta\sigma_p$ contributes significantly to the YS. In the calculation of $\Delta\sigma_p$ of small and large spherical particles, the shear and bypass mechanism are selected, respectively, and the $\Delta\sigma_{os}$ is dominant in the shear mechanism. The rod-shaped precipitates are equivalent to DWs, and the effect of $\Delta\sigma_g$ is calculated. In addition, when the temperature is reduced from 298 K to 77 K, the YS increment is quantitatively calculated, and the contribution of σ_0 is much higher than that

of other parts. Finally, the model is used to quantitatively predict the plasticity of Alloy C.

Acknowledgments

The authors would like to acknowledge the financial support of the Natural Science Foundation of Shanxi Province, China (Nos. 201901D111105 and 201901D111114), and the opening project of State Key Laboratory of Explosion Science and Technology (Beijing Institute of Technology), and the opening project number is KFJJ2013M. Atom probe tomography research was conducted by Dr. J.H. Luan and Dr. Z.B. Jiao at the Inter-University 3D Atom Probe Tomography Unit of City University of Hong Kong, which is supported by the CityU grant 9360161. P.K. Liaw appreciates support from (1) the National Science Foundation (DMR-1611180 and 1809640) with program directors, Drs. J. Yang, G. Shiflet, and D. Farkas and (2) the US Army Research Office (W911NF-13-1-0438 and W911NF-19-2-0049) with program managers, Drs. M.P. Bakas, S.N. Mathaudhu, and D.M. Stepp.

References

- [1] J.W. Yeh, S.K. Chen, S.J. Lin, J.Y. Gan, T.S. Chin, T.T. Shun, C.H. Tsau, S.Y. Chang, Nanostructured high-entropy alloys with multiple principal elements: Novel alloy design concepts and outcomes, *Advanced Engineering Materials* 6(5) (2004) 299-303.
- [2] J.W. Yeh, Alloy design strategies and future trends in high-entropy alloys, *JOM* 65(12) (2013) 1759-1771.
- [3] B. Cantor, I.T.H. Chang, P. Knight, A.J.B. Vincent, Microstructural development in equiatomic multicomponent alloys, *Materials Science and Engineering: A* 375-377 (2004) 213-218.
- [4] D.B. Miracle, O.N. Senkov, A critical review of high entropy alloys and related concepts, *Acta Materialia* 122 (2017) 448-511.
- [5] Y.F. Ye, Q. Wang, J. Lu, C.T. Liu, Y. Yang, High-entropy alloy: challenges and prospects, *Materials Today* 19(6) (2016) 349-362.
- [6] Y. Zhang, T.T. Zuo, Z. Tang, M.C. Gao, K.A. Dahmen, P.K. Liaw, Z.P. Lu, Microstructures and properties of high-entropy alloys, *Progress in Materials Science* 61 (2014) 1-93.
- [7] P.J. Shi, R.G. Li, Y. Li, Y.B. Wen, Y.B. Zhong, W.L. Ren, Z. Shen, T.X. Zheng, J.C. Peng, X. Liang, P.F. Hu, N. Min, Y. Zhang, Y. Ren, P.K. Liaw, D. Raabe, Y.D. Wang, Hierarchical crack buffering triples ductility in eutectic herringbone high-entropy alloys, *Science* 373(6557) (2021) 912-918.
- [8] X. Zeng, Z.Y. Liu, G.G. Wu, X. Tong, Y.Q. Xiong, X.D. Cheng, X.G. Wang, T. Yamaguchi, Microstructure and high-temperature properties of laser cladded AlCoCrFeNiTi_{0.5} high-entropy coating on Ti 6Al-4V alloy, *Surface and Coatings Technology* 418 (2021) 127243.
- [9] Z. Li, J.N. Qi, Z.Z. Li, H.X. Li, H. Xu, G.H. Bai, X.G. Liu, X.F. Zhang, Effect of grain and phase boundaries on soft magnetic properties of FeCoNiAlSi high-entropy alloys, *Materials Letters* 297 (2021) 129965.
- [10] Z.Q. Fu, W.P. Chen, H.M. Wen, D.L. Zhang, Z. Chen, B.L. Zheng, Y.Z. Zhou, E.J. Lavernia, Microstructure and strengthening mechanisms in an FCC structured single-phase nanocrystalline Co₂₅Ni₂₅Fe₂₅Al_{7.5}Cu_{17.5} high-entropy alloy, *Acta Materialia* 107 (2016) 59-71.

- [11] F. Granberg, K. Nordlund, M.W. Ullah, K. Jin, C. Lu, H. Bei, L.M. Wang, F. Djurabekova, W.J. Weber, Y. Zhang, Mechanism of radiation damage deduction in equiatomic multicomponent single phase alloys, *Physical Review Letters* 116(13) (2016) 135504.
- [12] Anonymous, superalloys: Alloying and performance, *Mechanical Engineering* 133(3) (2011) 52.
- [13] J.Y. He, W.H. Liu, H. Wang, Y. Wu, X.J. Liu, T.G. Nieh, Z.P. Lu, Effects of Al addition on structural evolution and tensile properties of the FeCoNiCrMn high-entropy alloy system, *Acta Materialia* 62(1) (2014) 105-113.
- [14] W.H. Liu, Y. Wu, J.Y. He, T.G. Nieh, Z.P. Lu, Grain growth and the Hall–Petch relationship in a high-entropy FeCrNiCoMn alloy, *Scripta Materialia* 68(7) (2013) 526-529.
- [15] T. Yang, Y.L. Zhao, W.P. Li, C.Y. Yu, J.H. Luan, D.Y. Lin, L. Fan, Z.B. Jiao, W.H. Liu, X.J. Liu, J.J. Kai, J.C. Huang, C.T. Liu, Ultrahigh-strength and ductile superlattice alloys with nanoscale disordered interfaces, *Science* 369(6502) (2020) 427-432.
- [16] P. Wang, Y.Q. Bu, J.B. Liu, Q.Q. Li, H.T. Wang, W. Yang, Atomic deformation mechanism and interface toughening in metastable high entropy alloy, *Materials Today* 37 (2020) 64-73.
- [17] W. Lu, C. Liebscher, F. Yan, X. Fang, Z. Li, Interfacial nanophases stabilize nanotwins in high-entropy alloys, *Acta Materialia* 185 (2020) 218-232.
- [18] W.J. Lu, C.H. Liebscher, F.K. Yan, X.F. Fang, L.L. Li, J.J. Li, W.Q. Guo, G. Dehm, D. Raabe, Z.M. Li, A TRIP-assisted dual-phase high-entropy alloy: Grain size and phase fraction effects on deformation behavior, *Acta Materialia* 131 (2017) 323-335.
- [19] Z.M. Li, F. Körmann, B. Grabowski, J. Neugebauer, D. Raabe, Ab initio assisted design of quinary dual-phase high-entropy alloys with transformation-induced plasticity, *Acta Materialia* 136 (2017) 262-270.
- [20] X.Z. Gao, Y.P. Lu, J.Z. Liu, J. Wang, T.M. Wang, Y.H. Zhao, Extraordinary ductility and strain hardening of Cr₂₆Mn₂₀Fe₂₀Co₂₀Ni₁₄ TWIP high-entropy alloy by cooperative planar slipping and twinning, *Materialia* 8 (2019) 100485.
- [21] T. Yang, Y.L. Zhao, W.H. Liu, J.J. Kai, C.T. Liu, L₁₂-strengthened high-entropy alloys for advanced structural applications, *Journal of Materials Research* 33(19) (2018) 2983-2997.
- [22] P. Pandey, S. Kashyap, D. Palanisamy, A. Sharma, K. Chattopadhyay, On the high temperature coarsening kinetics of γ' precipitates in a high strength

- $\text{Co}_{37.6}\text{Ni}_{35.4}\text{Al}_{9.9}\text{Mo}_{4.9}\text{Cr}_{5.9}\text{Ta}_{2.8}\text{Ti}_{3.5}$ fcc-based high entropy alloy, *Acta Materialia* 177 (2019) 82-95.
- [23] T. Yang, Y.L. Zhao, Y. Tong, Z.B. Jiao, J. Wei, J.X. Cai, X.D. Han, D. Chen, A. Hu, J.J. Kai, K. Lu, Y. Liu, C.T. Liu, Multicomponent intermetallic nanoparticles and superb mechanical behaviors of complex alloys, *Science* 362(6417) (2018) 933-937.
- [24] Y.L. Zhao, T. Yang, Y. Tong, J. Wang, J.H. Luan, Z.B. Jiao, D. Chen, Y. Yang, A. Hu, C.T. Liu, J.J. Kai, Heterogeneous precipitation behavior and stacking-fault-mediated deformation in a CoCrNi-based medium-entropy alloy, *Acta Materialia* 138 (2017) 72-82.
- [25] Y. Tong, D. Chen, D. B. Han, J. Wang, R. Feng, T. Yang, C. Zhao, Y.L. Zhao, W. Guo, Y. Shimizu, C.T. Liu, P.K. Liaw, K. Inoue, Y. Nagai, A. Hu, J.J. Kai, Outstanding tensile properties of a precipitation-strengthened FeCoNiCrTi_{0.2} high-entropy alloy at room and cryogenic temperatures, *Acta Materialia* 165 (2019) 228-240.
- [26] T. Yang, Y.L. Zhao, J.H. Luan, B. Han, J. Wei, J.J. Kai, C.T. Liu, Nanoparticles-strengthened high-entropy alloys for cryogenic applications showing an exceptional strength-ductility synergy, *Scripta Materialia* 164 (2019) 30-35.
- [27] Y. Yu, J. Wang, J. Li, H. Kou, W. Liu, Characterization of BCC phases in AlCoCrFeNiTi_x high entropy alloys, *Materials Letters* 138 (2015) 78-80.
- [28] M. Löbel, T. Lindner, T. Mehner, T. Lampke, Influence of titanium on microstructure, phase formation and wear behaviour of AlCoCrFeNiTi_x high-entropy alloy, *Entropy* 20(7) (2018) 505.
- [29] Q.S. Pan, L.X. Zhang, R. Feng, Q.H. Lu, K. An, A.C. Chuang, J.D. Poplawsky, D. Jonathan, P.K. Liaw, L. Lu, Gradient Cell Structured High-Entropy Alloy with Exceptional Strength and Ductility, *Science* (2021) eabj8114.
- [30] M.S. Lucas, G.B. Wilks, L. Mauger, J.A. Munoz, O.N. Senkov, E. Michel, J. Horwath, S.L. Semiatin, M.B. Stone, D.L. Abernathy, E. Karapetrova, Absence of long-range chemical ordering in equimolar FeCoCrNi, *Applied Physics Letters* 100(25) (2012) 251907.
- [31] I. Gutierrez-Urrutia, D. Raabe, Multistage strain hardening through dislocation substructure and twinning in a high strength and ductile weight-reduced Fe–Mn–Al–C steel, *Acta Materialia* 60(16) (2012) 5791-5802.

- [32] C.S. Whitcroft, J.W. Martin, The influence of chromium content on the precipitation of γ' (ordered Ni_3Ti) in some austenitic steels, *Materials Characterization* 2(4) (1969) 309-322.
- [33] D.H. Le, C. Colinet, P. Hicter, A. Pasturel, Theoretical description of phase equilibrium in the nickel-titanium system, *Journal of Physics: Condensed Matter* 3(50) (1991) 9965-9974.
- [34] H.P. Van, S.Y. Li, M. Seefeldt, L. Delannay, Deformation texture prediction: from the Taylor model to the advanced Lamel model, *International Journal of Plasticity* 21(3) (2005) 589-624.
- [35] A. Pasturel, C. Colinet, D.N. Manh, A.T. Paxton, M.V. Schilfsgaarde, Electronic structure and phase stability study in the Ni-Ti system, *Physical Review B* 52(21) (1995) 15176-15190.
- [36] Y.Z. Tian, L.J. Zhao, S. Chen, A. Shibata, Z.F. Zhang, N. Tsuji, Significant contribution of stacking faults to the strain hardening behavior of Cu-15%Al alloy with different grain sizes, *Scientific Reports* 5(1) (2015) 16707.
- [37] Y. Weng, H. Dong, Y. Gan, *Advanced steels: the recent scenario in steel science and technology*, 2011.
- [38] Z.J. Zhang, M.M. Mao, J.W. Wang, B. Gludovatz, Z. Zhang, S.X. Mao, E.P. George, Q. Yu, R.O. Ritchie, Nanoscale origins of the damage tolerance of the high-entropy alloy CrMnFeCoNi, *Nature Communications* 6(1) (2015) 10143.
- [39] Z. Wu, H. Bei, G.M. Pharr, E.P. George, Temperature dependence of the mechanical properties of equiatomic solid solution alloys with face-centered cubic crystal structures, *Acta Materialia* 81 (2014) 428-441.
- [40] S.Z. Niu, H.C. Kou, T. Guo, Y. Zhang, J. Wang, J.S. Li, Strengthening of nanoprecipitations in an annealed $\text{Al}_{0.5}\text{CoCrFeNi}$ high entropy alloy, *Materials Science and Engineering: A* 671 (2016) 82-86.
- [41] K.S. Ming, X.F. Bi, W. Jian, Realizing strength-ductility combination of coarse-grained $\text{Al}_{0.2}\text{Co}_{1.5}\text{CrFeNi}_{1.5}\text{Ti}_{0.3}$ alloy via nano-sized, coherent precipitates, *International Journal of Plasticity* 100 (2018) 177-191.
- [42] Y.L. Zhao, T. Yang, J.H. Zhu, D. Chen, Y. Yang, A. Hu, C.T. Liu, J.J. Kai, Development of high-strength Co-free high-entropy alloys hardened by nanosized precipitates, *Scripta Materialia* 148 (2018) 51-55.

- [43] A. Arlazarov, O. Bouaziz, A. Hazotte, M. Gouné, S. Allain, Characterization and modeling of manganese effect on strength and strain hardening of martensitic carbon steels, *ISIJ International* 53(6) (2013) 1076-1080.
- [44] B.B. He, B.M. Huang, S.H. He, Y. Qi, H.W. Yen, M.X. Huang, Increasing yield strength of medium Mn steel by engineering multiple strengthening defects, *Materials Science and Engineering: A* 724 (2018) 11-16.
- [45] A. Gali, E.P. George, Tensile properties of high-and medium-entropy alloys, *Intermetallics* 39 (2013) 74-78.
- [46] L. Kovarik, R.R. Unocic, L. Ju, P. Sarosi, C. Shen, Y. Wang, M.J. Mills, Microtwinning and other shearing mechanisms at intermediate temperatures in Ni-based superalloys, *Progress in Materials Science* 54(6) (2009) 839-873.
- [47] L. Fan, T. Yang, Y.L. Zhao, J.H. Luan, G. Zhou, H. Wang, Z.B. Jiao, C.T. Liu, Ultrahigh strength and ductility in newly developed materials with coherent nanolamellar architectures, *Nature communications* 11(1) (2020) 6240.
- [48] T. Yang, Y.L. Zhao, J.H. Luan, B. Han, J. Wei, J.J. Kai, C.T. Liu, Nanoparticles-strengthened high-entropy alloys for cryogenic applications showing an exceptional strength-ductility synergy, *Scripta Materialia* 164 (2019) 30-35.
- [49] M. Naeem, H.Y. He, F. Zhang, H.L. Huang, S. Harjo, T. Kawasaki, B. Wang, S. Lan, Z.D. Wu, F. Wang, Y. Wu, Z.P. Lu, Z.W. Zhang, C.T. Liu, X.L. Wang, Cooperative deformation in high-entropy alloys at ultralow temperatures, *Science Advances* 6(13) (2020) eaax4002.
- [50] S.J. Chen, H.S. Oh, B. Gludovatz, S.J. Kim, E.S. Park, Z. Zhang, R.O. Ritchie, Q. Yu, Real-time observations of TRIP-induced ultrahigh strain hardening in a dual-phase CrMnFeCoNi high-entropy alloy, *Nature Communications* 11(1) (2020) 826.
- [51] G. Laplanche, A. Kostka, O.M. Horst, G. Eggeler, E.P. George, Microstructure evolution and critical stress for twinning in the CrMnFeCoNi high-entropy alloy, *Acta Materialia* 118 (2016) 152-163.
- [52] Y.Q. Wang, B. Liu, K. Yan, M.S. Wang, S. Kabra, Y.L. Chiu, D. Dye, P.D. Lee, Y. Liu, B. Cai, Probing deformation mechanisms of a FeCoCrNi high-entropy alloy at 293 and 77 K using in situ neutron diffraction, *Acta Materialia* 154 (2018) 79-89.

- [53] A. Araki, E. Kobayashi, T. Sato, W. Poole, Deformation Twinning Behavior in Precipitate Strengthened Cu-Ni-Si Alloys, TMS 2015 144th Annual Meeting & Exhibition, (2015) 491-496.
- [54] Y.F. Shen, Y.D. Wang, X.P. Liu, X. Sun, R.L. Peng, S.Y. Zhang, L. Zuo, P.K. Liaw, Deformation mechanisms of a 20Mn TWIP steel investigated by in situ neutron diffraction and TEM, *Acta Materialia* 61(16) (2013) 6093-6106.
- [55] A.J. Ardell, Precipitation hardening, *Metallurgical Transactions A* 16(12) (1985) 2131-2165.
- [56] G.I. Taylor, The mechanism of plastic deformation of crystals. Part I.—Theoretical, *Proceedings of the Royal Society of London. Series A, Containing Papers of a Mathematical and Physical Character* 145(855) (1934) 362-387.
- [57] T.M. Pollock, A.S. Argon, Creep resistance of CMSX-3 nickel base superalloy single crystals, *Acta Metallurgica Et Materialia* 40(1) (1992) 1-30.
- [58] R.W. Kozar, A. Suzuki, W.W. Milligan, J.J. Schirra, M.F. Savage, T.M. Pollock, Strengthening mechanisms in polycrystalline multimodal nickel-base superalloys, *Metallurgical and Materials Transactions A* 40(7) (2009) 1588-1603.
- [59] M.E. Dalen, T. Gyger, D.C. Dunand, D.N. Seidman, Effects of Yb and Zr microalloying additions on the microstructure and mechanical properties of dilute Al-Sc alloys, *Acta Materialia* 59(20) (2011) 7615-7626.
- [60] H.W. Zhang, P.Z. Liu, J.X. Hou, J.W. Qiao, Y.C. Wu, Prediction of Strength and Ductility in Partially Recrystallized CoCrFeNiTi_{0.2} High-Entropy Alloy, *Entropy* 21(4) (2019) 389.
- [61] M.X. Yang, D.S. Yan, F.P. Yuan, P. Jiang, E. Ma, X.L. Wu, Dynamically reinforced heterogeneous grain structure prolongs ductility in a medium-entropy alloy with gigapascal yield strength, *Proceedings of the National Academy of Sciences* 115(28) (2018) 7224.
- [62] Y.H. Jo, W.M. Choi, S.S. Sohn, H.S. Kim, B.J. Lee, S. Lee, Role of brittle sigma phase in cryogenic-temperature-strength improvement of non-equi-atomic Fe-rich VCrMnFeCoNi high entropy alloys, *Materials Science and Engineering: A* 724 (2018) 403-410.
- [63] D.Y. Li, C.X. Li, T. Feng, Y.D. Zhang, G. Sha, J.J. Lewandowski, P.K. Liaw, Y. Zhang, High-entropy Al_{0.3}CoCrFeNi alloy fibers with high tensile strength and ductility at ambient and cryogenic temperatures, *Acta Materialia* 123 (2017) 285-294.

- [64] P. Sathiyamoorthi, J. Moon, J.W. Bae, P. Asghari-Rad, H.S. Kim, Superior cryogenic tensile properties of ultrafine-grained CoCrNi medium-entropy alloy produced by high-pressure torsion and annealing, *Scripta Materialia* 163 (2019) 152-156.
- [65] G. Laplanche, P. Gadaud, C. Bärsch, K. Demtröder, C. Reinhart, J. Schreuer, E.P. George, Elastic moduli and thermal expansion coefficients of medium-entropy subsystems of the CrMnFeCoNi high-entropy alloy, *Journal of Alloys and Compounds* 746 (2018) 244-255.
- [66] R.L. Fleischer, Substitutional solution hardening, *Acta Metallurgica* 11(3) (1963) 203-209.
- [67] V.R. Manga, S.L. Shang, W.Y. Wang, Y. Wang, J. Liang, V.H. Crespi, Z.K. Liu, Anomalous phonon stiffening associated with the (111) antiphase boundary in $L1_2$ Ni₃Al, *Acta Materialia* 82 (2015) 287-294.
- [68] T.W. Clyne, P.J. Withers, *An Introduction to metal matrix composites, An Introduction to Metal Matrix Composites* 1995.
- [69] N. Chawla, K.K. Chawla, Metal-matrix composites in ground transportation, *JOM* 58(11) (2006) 67-70.
- [70] A.F. Whitehouse, T.W. Clyne, Cavity formation during tensile straining of particulate and short fibre metal matrix composites, *Acta Metallurgica et Materialia* 41(6) (1993) 1701-1711.

Tables:

Table 1

Grain sizes, diameters, and volume fractions of two kinds of spherical particles for three alloys.

Alloy	Grain size (μm)	Diameter of particles (nm)	Volume fraction (%)
Homogenized	54		
Aged	71	16.5	6.79
Recrystallized	7	Ds = 6.5 DI = 200	3.95 10

Table 2

Chemical compositions of different phases by the 3D-APT analysis (at. %).

Element	Matrix	Small spherical precipitates	Rod-shaped precipitates
Co	24.68 \pm 0.21	16.82 \pm 0.40	15.73 \pm 0.25
Cr	25.30 \pm 0.21	2.03 \pm 0.15	2.18 \pm 0.10
Fe	27.08 \pm 0.22	2.54 \pm 0.17	2.50 \pm 0.11
Ni	20.60 \pm 0.20	54.61 \pm 0.54	55.75 \pm 0.34
Ti	2.35 \pm 0.08	24.00 \pm 0.46	23.84 \pm 0.29

Table 3

The yield strengths, ultimate tensile strengths, and elongations of three alloys at 298 K.

Alloy	YS (MPa)	UTS (MPa)	EL (%)
Homogenized	280	650	47
Aged	580	950	27
Recrystallized	720	1,085	30

Table 4

The yield strengths, ultimate tensile strengths, and elongations of three alloys at 77 K.

Alloy	YS (MPa)	UTS (MPa)	EL (%)
Homogenized	400	785	60
Aged	650	990	35
Recrystallized	1,000	1,500	35

Table 5

The strengthening contributions of various precipitates in Alloy B.

Alloy	$\Delta \sigma$ coherency (MPa)	$\Delta \sigma$ modulus (MPa)	$\Delta \sigma$ coherency+ $\Delta \sigma$ modulus (MPa)	$\Delta \sigma$ order (MPa)	Experimental strength increment (MPa)
Alloy B	127.7	32.2	160.9	281.3	300

Table 6

The strengthening contributions of various precipitates in Alloy C.

Alloy (Type of particles)	$\Delta \sigma$ coherency (MPa)	$\Delta \sigma$ modulus (MPa)	$\Delta \sigma$ coherency+ $\Delta \sigma$ modulus (MPa)	$\Delta \sigma$ order (MPa)	$\Delta \sigma$ rowan (MPa)	Experimental strength increment (MPa)
Small spherical particles	60.5	19.4	79.9	212.7	-	440
Large spherical particles	-	-	-	-	155.7	

Figure Captions:

Fig. 1. XRD patterns and SEM micrographs of Alloy A (a,d), Alloy B (b,e), Alloy C (c,f), (e₁) An enlarged view of the small spherical particles morphology for Alloy B.

Fig. 2. EBSD images of Alloy A (a), Alloy B (b), Alloy C (c), (d) Grain-boundary image of Alloy C contains twin boundaries (red lines) (TD: transverse direction, LD: longitudinal direction).

Fig. 3. Bright-field TEM images of the three kinds of precipitates (a, b, and c); (d) An enlarged view of the small spherical particles morphology for Alloy C; SAED patterns taken from the rod-shaped precipitate (a₁), large spherical particle (a₂), and small spherical particles (d₁); High-resolution TEM images showing the interface between the fcc matrix and rod-shaped precipitate (b₁) and large spherical particle (c₁) with their relative FFT and IFFT patterns are shown in (b₂ and b₃) and (c₂ and c₃), respectively.

Fig. 4. Schematic diagrams of microstructures for Alloy A (a), Alloy B (b), and Alloy C (c).

Fig. 5. Schematic demonstration of the transformation of the L1₂ to η phase.

Fig. 6. Co, Cr, Fe, Ni, and Ti atom maps and 35 at.% Ni iso-surface showing the outline of precipitates for Alloy B (a) and Alloy C (c); Proximity histogram constructed across the interface between the matrix and precipitates for Alloy B (b) and Alloy C (c).

Fig. 7. Representative engineering stress-strain curves of three alloys at 298 K (a) and 77 K (b); (c) Strain-hardening rate ($d\sigma/d\varepsilon$) versus true strain of Alloy C at 298 K and 77 K; (d) DIC maps showing the strain distributions prior to the fracture of Alloy C.

Fig. 8. The maps of ultimate tensile strength versus total elongation (a) and yield strength versus product of strength and elongation (b) of some traditional alloys, advanced steels, commercial superalloys, HEAs, or MEAs, including Alloy C at 298 K and 77 K.

Fig. 9. Bright-field TEM images of Alloy C deformed at 298 K.

Fig. 10. Bright-field TEM images of the microstructure of Alloy C deformed at 77 K. (a) Interactions among dislocations, SFs, and precipitates; (e) L-C locks; (f) Dislocations bypass the large spherical particle.

Fig. 11. (a) True stress-strain curves of Alloy C at 77 K and 298 K; (b) Stacking fault energy of the matrix alloy at 77 K and 298 K, and $u_x = 1$ represents a Burgers vector; Molecular dynamics simulation diagrams of an initial structure (c,e) and stacking fault (d,f) for the matrix alloy at 77 K.

Fig. 12. Schematic illustrations showing that the rod-shaped precipitates are equivalent to the sub-grain boundary.

Fig. 13. Contributions of different strengthening mechanisms and comparison between theoretical and experimental values at 298 K and 77 K.

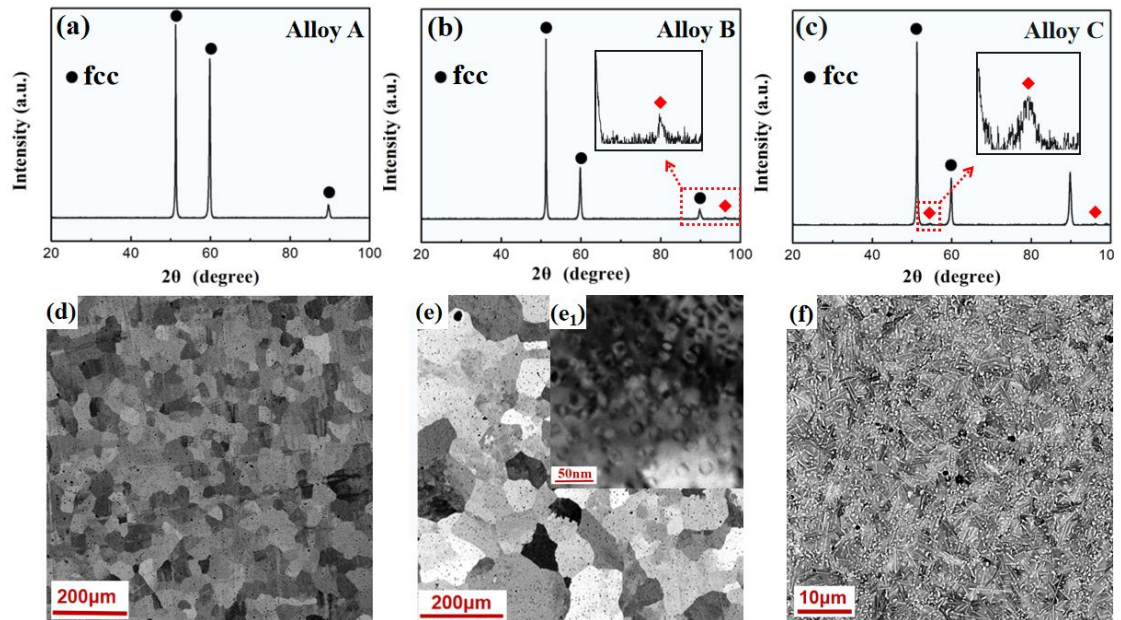


Fig. 4. XRD patterns and SEM micrographs of Alloy A (a,d), Alloy B (b,e), Alloy C (c,f), (e₁) An enlarged view of the small spherical particles morphology for Alloy B.

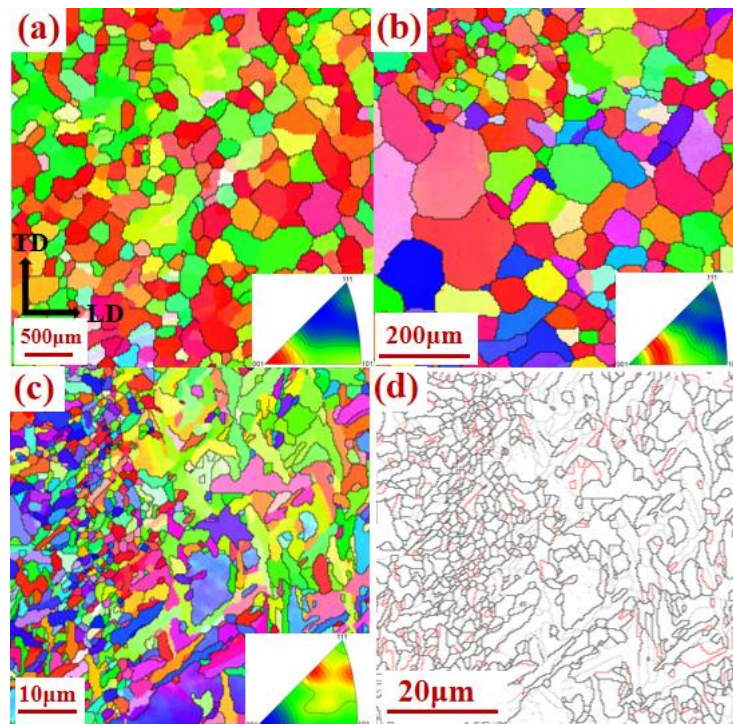


Fig. 5. EBSD images of Alloy A (a), Alloy B (b), Alloy C (c), (d) Grain-boundary image of Alloy C contains twin boundaries (red lines) (TD: transverse direction, LD: longitudinal direction).

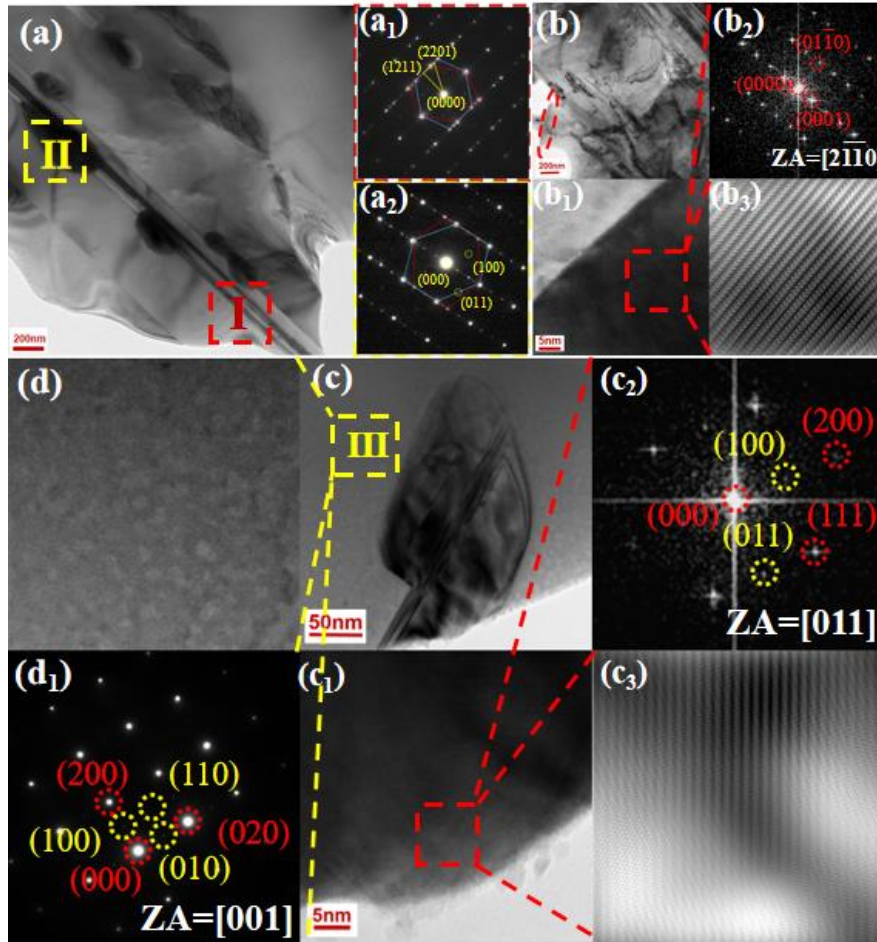


Fig. 6. Bright-field TEM images of the three kinds of precipitates (a, b, and c); (d) An enlarged view of the small spherical particles morphology for Alloy C; SAED patterns taken from the rod-shaped precipitate (a₁), large spherical particle (a₂), and small spherical particles (d₁); High-resolution TEM images showing the interface between the fcc matrix and rod-shaped precipitate (b₁) and large spherical particle (c₁) with their relative FFT and IFFT patterns are shown in (b₂ and b₃) and (c₂ and c₃), respectively.

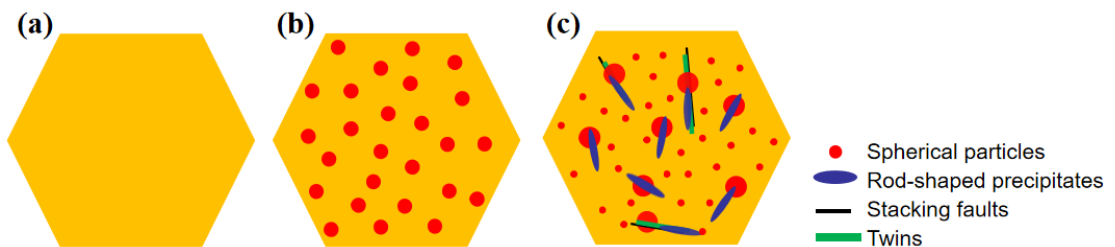


Fig. 4. Schematic diagrams of microstructures for Alloy A (a), Alloy B (b), and Alloy C (c).

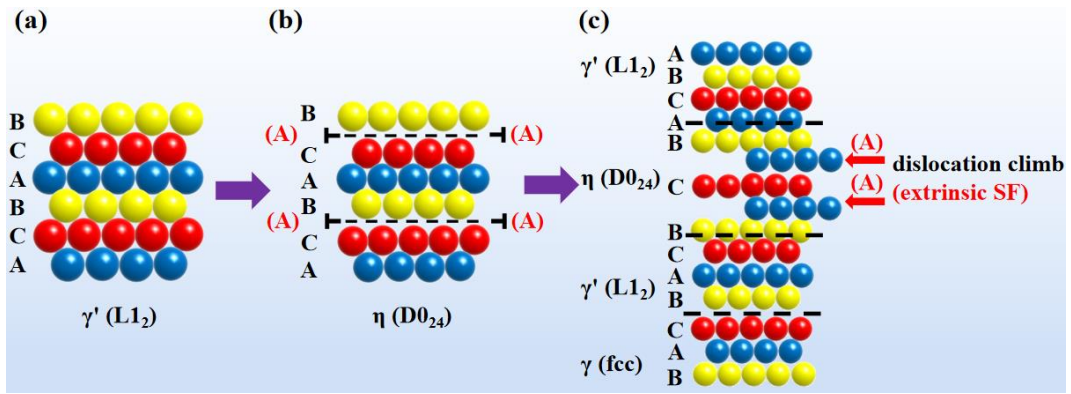


Fig. 5. Schematic demonstration of the transformation of the $L1_2$ to η phase.

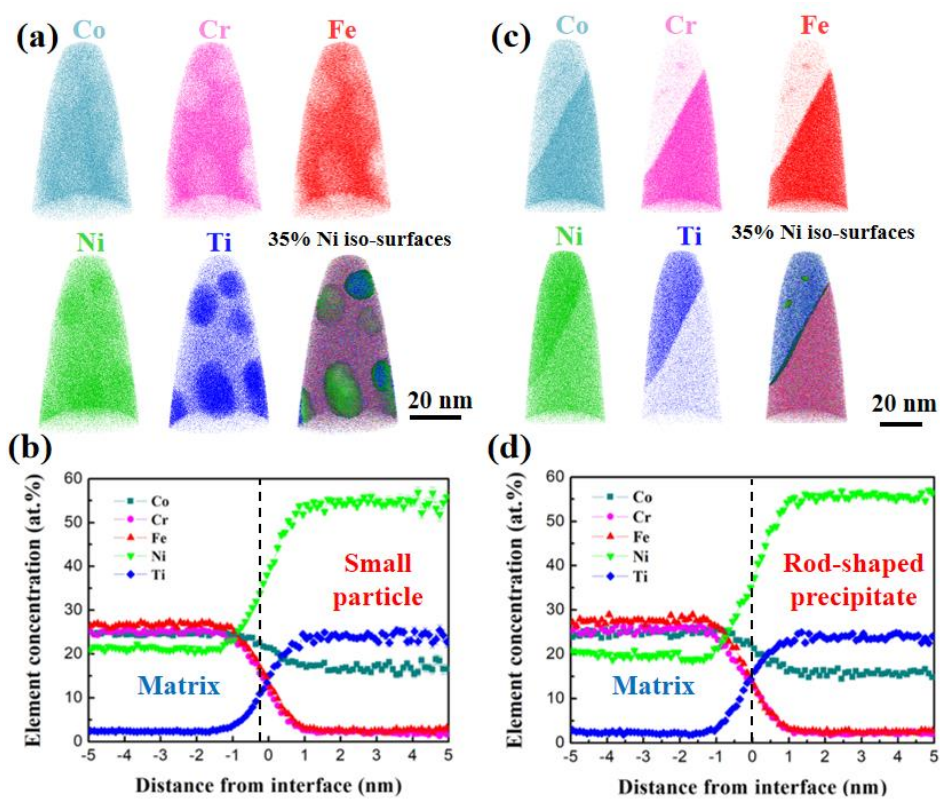


Fig. 6. Co, Cr, Fe, Ni, and Ti atom maps and 35 at.% Ni iso-surface showing the outline of precipitates for Alloy B (a) and Alloy C (c); Proximity histogram constructed across the interface between the matrix and precipitates for Alloy B (b) and Alloy C (d).

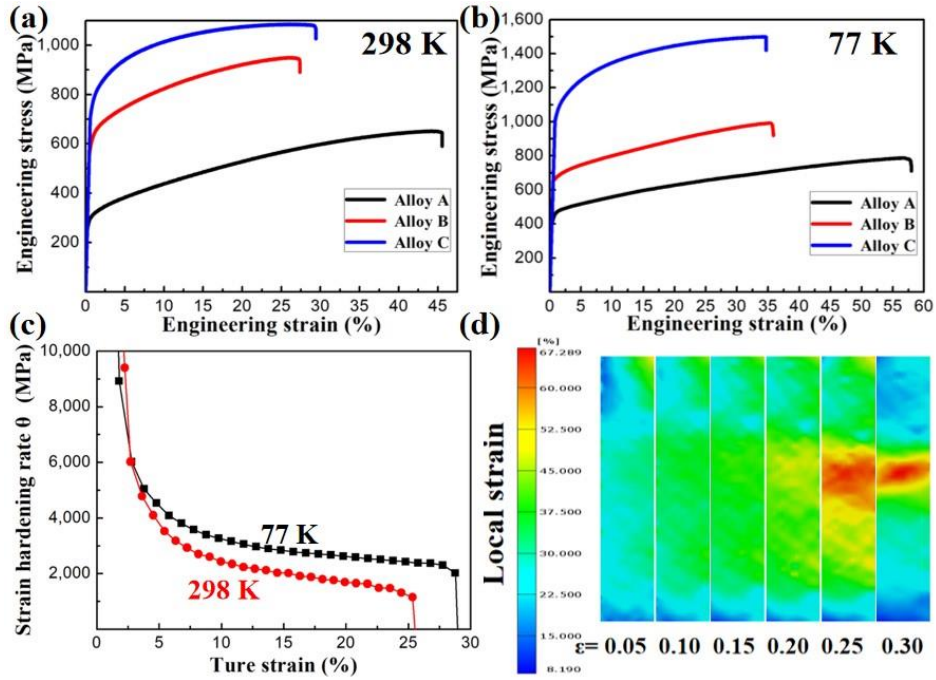


Fig. 7. Representative engineering stress-strain curves of three alloys at 298 K (a) and 77 K (b); (c) Strain-hardening rate ($d\sigma/d\varepsilon$) versus true strain of Alloy C at 298 K and 77 K; (d) DIC maps showing the strain distributions prior to the fracture of Alloy C.

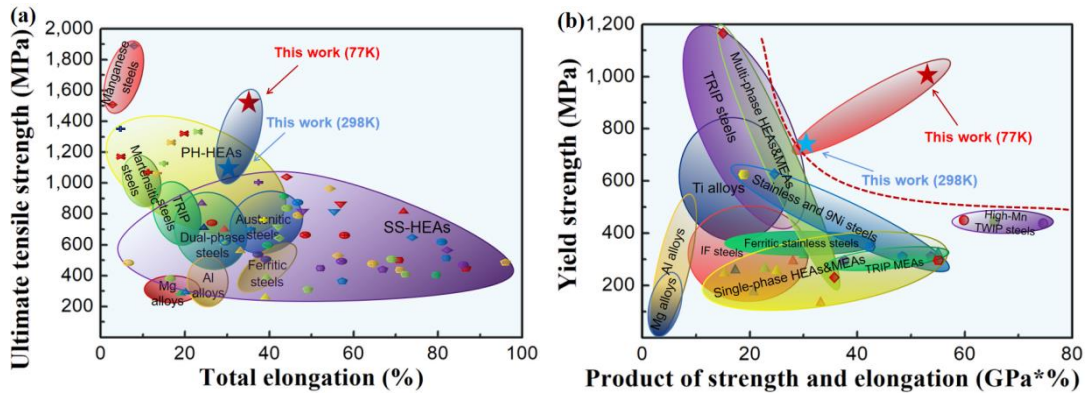


Fig. 8. The maps of ultimate tensile strength versus total elongation (a) and yield strength versus product of strength and elongation (b) of some traditional alloys, advanced steels, commercial superalloys, HEAs, or MEAs, including Alloy C at 298 K and 77 K.

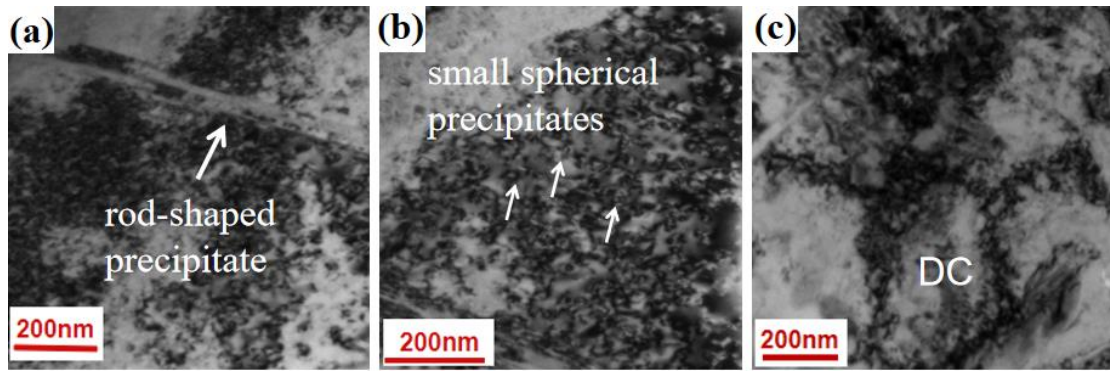


Fig. 9. Bright-field TEM images of Alloy C deformed at 298 K.

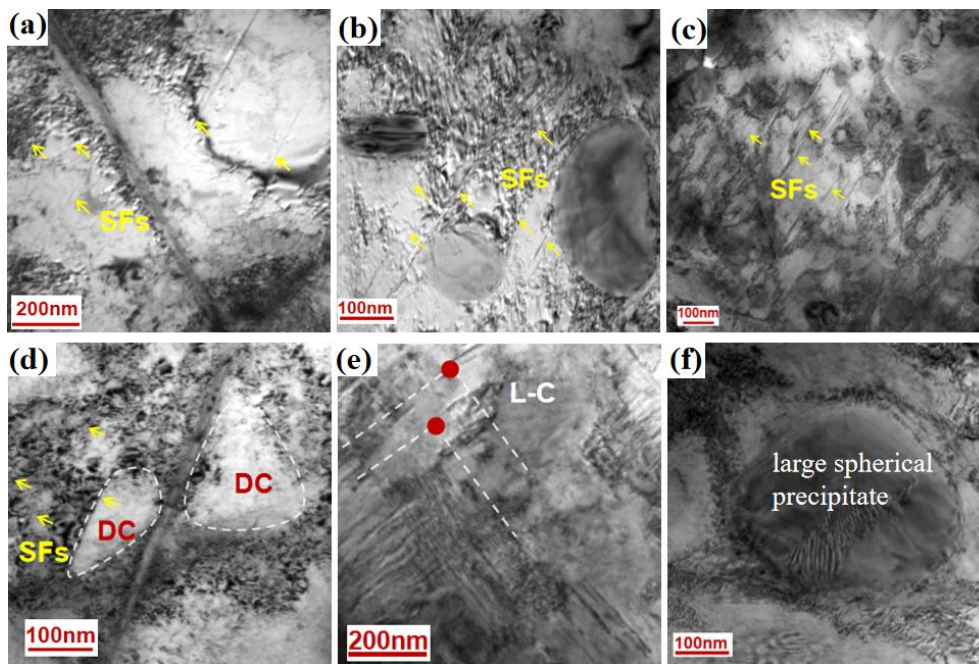


Fig. 10. Bright-field TEM images of the microstructure of Alloy C deformed at 77 K. (a) Interactions among dislocations, SFs, and precipitates; (e) L-C locks; (f) Dislocations bypass the large spherical particle.

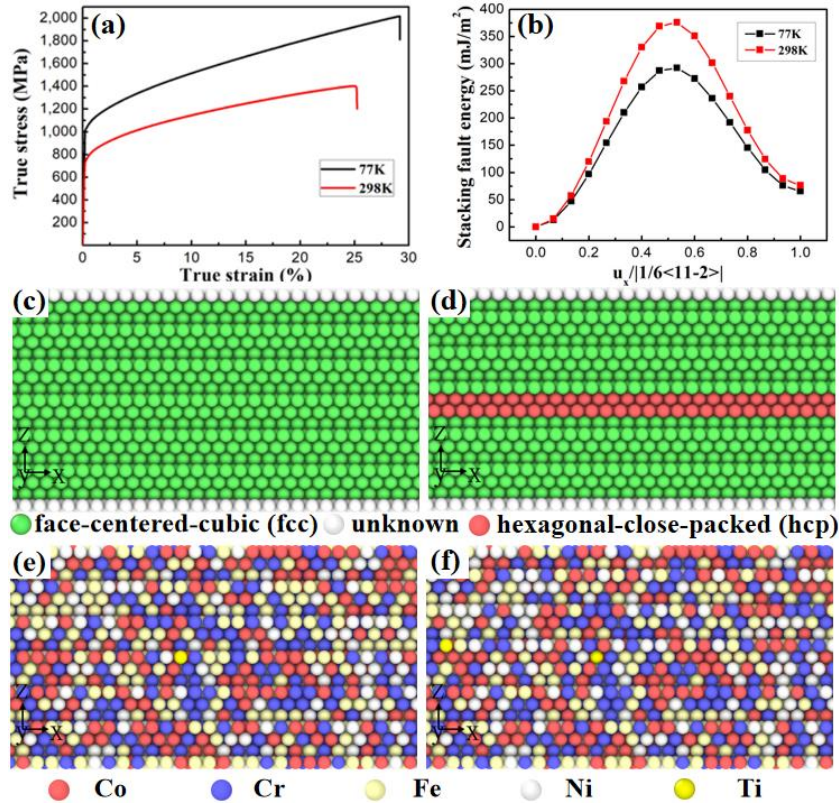


Fig. 11. (a) True stress-strain curves of Alloy C at 77 K and 298 K; (b) Stacking fault energy of the matrix alloy at 77 K and 298 K, and $u_x = 1$ represents a Burgers vector; Molecular dynamics simulation diagrams of an initial structure (c,e) and stacking fault (d,f) for the matrix alloy at 77 K.

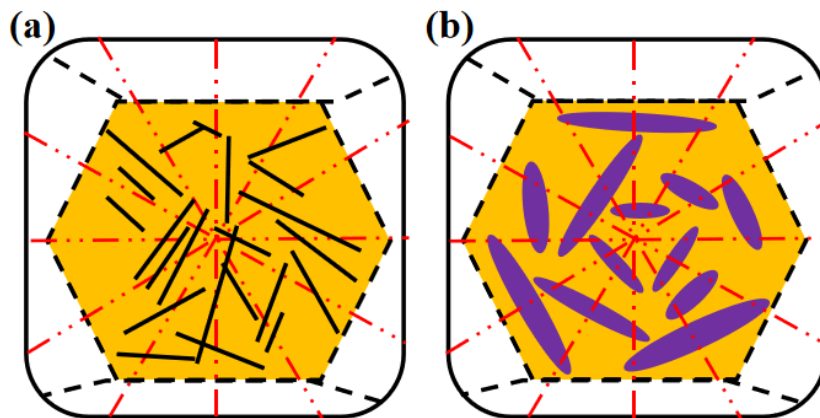


Fig. 12. Schematic illustrations showing that the rod-shaped precipitates are equivalent to the sub-grain boundary.

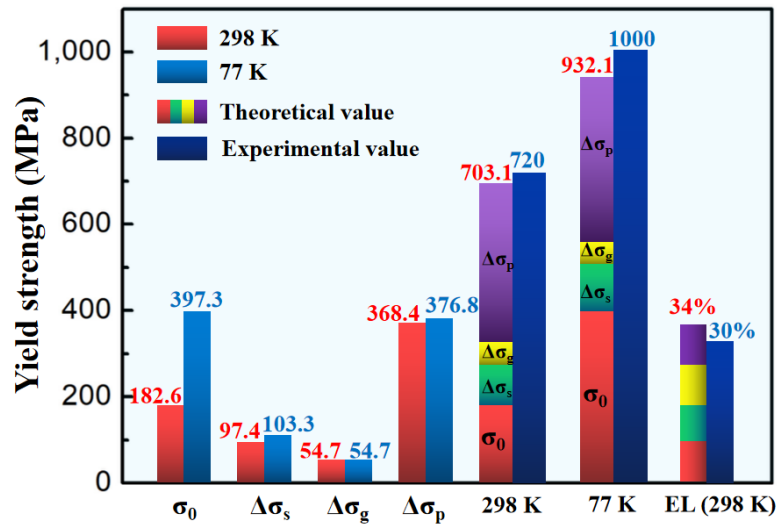


Fig. 13. Contributions of different strengthening mechanisms and comparison between theoretical and experimental values at 298 K and 77 K.